ACS APPLIED MATERIALS & INTERFACES

Research Article

www.acsami.org

Graphene Quantum Dots Embedded in Bi_2Te_3 Nanosheets To Enhance Thermoelectric Performance

Shuankui Li,[†,§] Tianju Fan,[†,§] Xuerui Liu,[†] Fusheng Liu,[‡] Hong Meng,[†] Yidong Liu,*[,†] and Feng Pan*[,†]

[†]School of Advanced Materials, Peking University Shenzhen Graduate School, Shenzhen 518055, China

[‡]College of Materials Science and Engineering, Shenzhen University and Shenzhen Key Laboratory of Special Functional Materials, Shenzhen 518060, China

Supporting Information

ABSTRACT: Novel Bi_2Te_3/graphene quantum dots (Bi_2Te_3/GQDs) hybrid nanosheets with a unique structure that GQDs are homogeneously embedded in the Bi_2Te_3 nanosheet matrix have been synthesized by a simple solution-based synthesis strategy. A significantly reduced thermal conductivity and enhanced powder factor are observed in the Bi_2Te_3/GQDs hybrid nanosheets, which is ascribed to the optimized thermoelectric transport properties of the Bi_2Te_3/GQDs interface. Furthermore, by varying the size of the GQDs, the thermoelectric performance of Bi_2Te_3/GQDs hybrid nanostructures could be further enhanced, which could be attributed to the optimization of the density and dispersion manner of the GQDs in the Bi_2Te_3 matrix. A maximum ZT of 0.55 is obtained at 425 K for the Bi_2Te_3/GQDs-20 nm, which is higher than that of Bi_2Te_3 without hybrid nanostrucure. This work provides insights for the structural design and synthesis of Bi_2Te_3-based hybrid thermoelectric materials, which will be important for future development of broadly functional material systems.

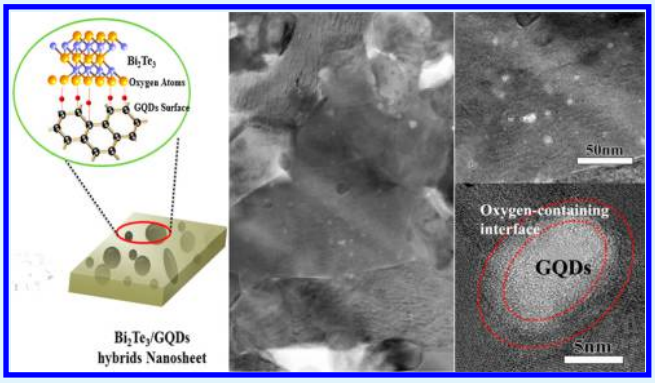

KEYWORDS: *thermoelectric materials, graphene quantum dot, hybrid nanostructure, charged interface, phonon scattering*

1. INTRODUCTION

Bismuth telluride and its solid solutions are some of the most efficient thermoelectric materials near room temperature, but they are still not widely applied in useable thermoelectric devices because of their poor energy conversion efficiency.[1−3] The conversion efficiency is characterized by the dimensionless figure-of-merit ZT = $(S^2\sigma/\kappa)T$, where S, σ, κ, and T are the Seebeck coefficient, electrical conductivity, total thermal conductivity, and absolute temperature, respectively. Obviously, an excellent thermoelectric material should have a large power factor ($S^2\sigma$) as well as low thermal conductivity, which is difficult to achieve in a conventional material because of the interdependence of these three physical parameters.[4,5] However, with the decreasing of the material dimensionality from conventional micrometer to nanometer, the new variable of length scale becomes available for controlling the thermoelectric properties of materials, which might allow new opportunities to optimize the three physical parameters independently. Extensive efforts have been made to controllably synthesize Bi_2Te_3-based nanostructures. Various nanomaterials, such as nanowires,[6] nanorods,[7] nanoplates/nanosheets,[8] and nanoheterostructures, have been developed to improve their thermoelectric performances.[9,10] Moreover, a constructed hybrid nanostructure with a domain size comparable to or smaller than the mean free path and/or coherence length of the carriers is another promising way to realize the ballistic/coherent transport of heat and charge carriers. Unfortunately, limited work has been reported on the design and synthesis of Bi_2Te_3-based hybrid nanostructures with well-controlled components and interfaces to achieve simultaneously large power factor and low thermal conductivity.

Graphene quantum dots (GQDs), a class of zero-dimensional carbon nanoparticles with typical dimensions of approximately less than 20 nm, have become a newly emerging material for various applications not only due to their appealing characteristics, such as high surface area, potential biocompatibility or low toxicity, and the availability of a $\pi-\pi$ conjugated network with functionalizable surface groups,[11,12] but also due to their unique quantum confinement and edge effects.[13,14] Therefore, the design and fabrication of Bi_2Te_3/GQDs hybrid materals seem to be a potential strategy for exploring novel thermoelectric materials with optimized carrier and phonon transport performance. The introduction of GQDs with domain sizes comparable to or smaller than the mean free

Received: November 8, 2016
Accepted: January 10, 2017
Published: January 10, 2017

DOI: 10.1021/acsami.6b14274
ACS Appl. Mater. Interfaces 2017, 9, 3677−3685

path and/or coherence length of the carriers would introduce quantum-confinement effects to enhance the thermoelectric performance. In addition to the quantum confinement effect of electrons, the designed high-density Bi_2Te_3/GQDs interfaces would impose strong boundary scatterings on phonons and reduce the thermal conductivity.[15,16] Furthermore, compared to conventional approaches, such as atomic defects and modulation doping, the strategy provides more degrees of freedom in scattering engineering, such as the size, interface composition, and spatial distribution of the GQDs, which could be used to further modulate carrier and phonon transport characteristics.

In this study, we proposed a new recipe to design and fabricate Bi_2Te_3/GQDs hybrid nanosheets, in which GQDs are homogeneously embedded in the Bi_2Te_3 nanosheet matrix, via a simple solution-based synthesis strategy. This study reveals that the charged Bi_2Te_3/GQDs interface could affect the carrier transport behavior by the modification of the carrier concentration and mobility, while effectively scattering phonons across integrated length scales leading to very low lattice thermal conductivities. The ZT value of the Bi_2Te_3/GQDs hybrid is 1.6 times higher than that of Bi_2Te_3, which could be further improved by adjusting the size of the GQDs. This work provides the insight for the structural design and synthesis of Bi_2Te_3-based hybrid thermoelectric materials, which will be important for future development of broadly functional material systems.

2. EXPERIMENTAL SECTION

2.1. Materials. TeO_2 powder (99.999%), $Bi(NO_3)_3{\cdot}5H_2O$, sodium hydroxide, vitamin C, ethylene glycol, acetone, and ethanol were purchased from the Shanghai Reagent Company. All the chemicals were used as obtained without further purification.

2.2. Synthesis of the Bi_2Te_3/GQDs Nanosheet. For the synthesis of the Bi_2Te_3/GQDs hybrid nanosheet, 2.40 g of NaOH and 1.92 g of TeO_2 powder were added into 60 mL of ethylene glycol in a three-neck flask equipped with a standard Schlenk line to yield a transparent Te precursor solution. For the synthesis of the Bi precursor solution, 3.88 g of $Bi(NO_3)_3{\cdot}5H_2O$ and 0.53 g of vitamin C were added into another 20 mL of ethylene glycol under magnetic stirring to yield a transparent Bi precursor solution. Then, an amount of GQDs solution (4 mg/mL) was added into the as-prepared Bi precursor solution under magnetic stirring. For the synthesis of the Bi_2Te_3/GQDs hybrid nanosheet, the three-neck flask was heated to 160 °C under nitrogen, and then, the as-prepared Bi precursor solution was injected into the above solution at 160 °C. After reaction for another 2 h, the products were precipitated with ethanol and deionized water several times and then dried at 60 °C for 24 h.

2.3. Characterization. X-ray diffraction (XRD) was performed on a Bruker D8 Advance powder X-ray diffractometer; field-emission scanning electron microscopy (FE-SEM) was performed on a Zeiss SUPRA-55; transmission electron microscopy (TEM) was performed on a JEOL-2010 instrument. X-ray photoelectron spectroscopy (XPS) spectra were acquired on a Thermo Fisher ESCALAB 250X surface analysis system equipped with a monochromatized Al anode X-ray source ($h\nu$ = 1486.6 eV).

2.4. Thermoelectric Measurements. The dry powders were pressed into pellets by spark plasma sintering (SPS) at 350 °C for 5 min under vacuum with a uniaxial pressure of 50 MPa. The pellets were cylinders 10 mm in diameter and 14 mm in height. In order to ensure the thermoelectric property measurement was conducted along the same direction, a disk with thickness of around 2 mm was cut from the sintered pellets to measure the thermal conductivity, and a cuboid about 3 mm × 3 mm × 12 mm was cut from the remaining part of the sintered pellet to measure the values of σ and S. The electrical conductivity and Seebeck coefficient were simultaneously measured using a ULVAC ZEM-3 within the temperature range 300−480 K. The thermal conductivity (κ) was calculated using the equation $\kappa = DC_p\rho$, where D, C_p, and ρ are the thermal diffusivity coefficient, specific heat capacity, and density, respectively. The thermal diffusivity coefficient was measured by a laser flash apparatus using Netzsch LFA 457 from 300 to 480 K, the specific heat (C_p) was tested by a differential scanning calorimeter (Mettler DSC1), and the density (ρ) was calculated by using the mass and dimensions of the pellet.

3. RESULTS AND DISCUSSION

In this study, we demonstrate a surfactant-free colloidal method toward the preparation of the Bi_2Te_3/GQDs hybrid nanosheet, and the scheme is shown in Figure 1. In a typical procedure, a

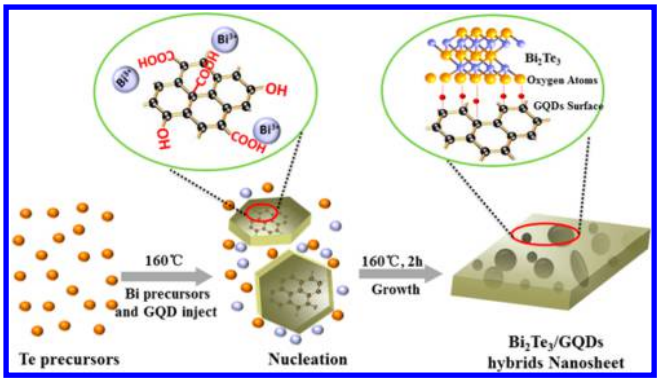

Figure 1. Solution synthesis process and formation mechanism of the Bi_2Te_3/GQDs hybrid nanosheet.

GQDs solution (4 mg/mL) was first prepared as described in a previous report (Figure S1).[17] The Te precursors containing stoichiometric amounts of TeO_2 and NaOH and the transparent Bi precursors solution containing stoichiometric amounts of $Bi(NO_3)_3{\cdot}5H_2O$, vitamin C, and GQDs solution were prepared, respectively. The reaction is triggered at 165 °C by rapid injection of the Bi precursors solution into the Te precursors solution in a three-neck flask, and the initially transparent mixture turns dark purple immediately after injection. As previously reported, there are a large number of oxygen-containing functional groups (−OH and −COOH) on the surface of GQDs, which might provide tight chemical bonding with transition metal ions.[18,19] Thus, for the synthesis of the Bi_2Te_3/GQDs hybrid nanosheet, through the coordinate interaction, the Bi ion could be easily absorbed on the GQDs first. Therefore, at the reaction stage, the nucleation and subsequent growth of Bi_2Te_3 is selective on surfaces of GQDs, which is confirmed by the fact that the GQDs uniformly dispersed in the Bi_2Te_3 nanosheet matrix. It should be pointed out that the initial GQDs would be reduced under the reaction condition, which was confirmed by XPS analysis.

The morphology and microstructure of the as-prepared Bi_2Te_3/GQDs hybrid nanosheets were studied by SEM and TEM. The SEM images (Figure 2a, b) reveal that irregular Bi_2Te_3/GQDs hybrid nanosheets with a thickness of about 10 nm have been prepared. The products preferentially grow into two-dimensional structures, which should be attributed to the intrinsically anisotropic bonding nature due to the weak van der Waals interaction along the c axis. Compared to the sample prepared without adding the GQDs (Figure S2), the morphology shows a discernible change, which could be ascribed to the small amount of GQDs. From the high-resolution TEM (HR-TEM) image (Figure 2d), the nonuni-

DOI: 10.1021/acsami.6b14274
ACS Appl. Mater. Interfaces 2017, 9, 3677−3685

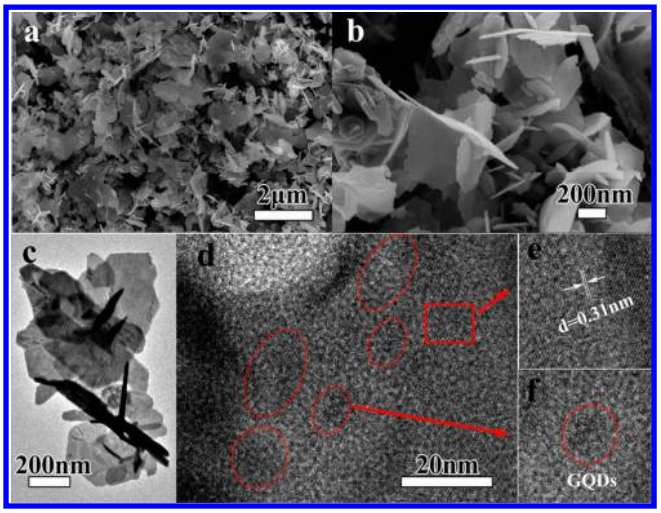

Figure 2. (a, b) SEM images of the Bi_2Te_3/GQDs hybrid nanosheet; (c, d) TEM images, where the red regions indicate the GQDs; (e, f) HR-TEM images of the Bi_2Te_3 and GQDs regions, respectively.

form contrast and crystallinity range about 5−10 nm (in the red frame) indicate that the chemical constituent is nonuniform. Considering the synthesis strategy, the nonuniform range corresponds to the GQDs, which is further confirmed by HR-TEM images. It is found that there are two distinct regions, which could be attributed to the GQDs region and the as-grown Bi_2Te_3 region, respectively. The GQDs region in the red frame (Figure 2f) about 5−10 nm reveals an amorphous nature. Interesting, the Bi_2Te_3/GQDs interface reveals atomically disordered regions of about 5 nm, which correspond to the oxygen-containing interface near the GQDs surface and are confirmed by XPS.

The Bi_2Te_3/GQDs hybrid nanosheets with different GQDs contents, denoted as Bi_2Te_3/GQDs*x* (*x* is the volume of GQDs solution (4 mg/mL)) have been characterized by XRD. Figure 3a shows the typical XRD pattern of the as-prepared sample, which can be indexed to the rhombohedra structured Bi_2Te_3 phase (space group: $R\bar{3}m$, JCPDS data card no.15-0863). The peaks are quite broad mainly due to the small crystal size of the as-prepared products. By comparing the XRD patterns of the samples after SPS sintering with their corresponding powders, it is noted that one more weak peak near 30° appeared, which may be related to the oxidation of Bi_2Te_3 on the Bi_2Te_3/GQDs interface. As the content of GQDs increased from 1 to 4 mL, the broadening and weakening XRD patterns reveal the significant randomness of the grains, which were confirmed by the SEM images of the fractured surfaces after the SPS process. As shown in Figure S3, all samples possess a well-crystallized and void-free feature, which is consistent with their high density (Table S1). Moreover, it should be noted that the nanograins are about 20−30 nm without apparent preferential orientation, which are smaller than those of pure Bi_2Te_3. The grain sizes become smaller with the increased GQDs content implying that the oxygen-containing interface and disorder could suppress the grain growth at the SPS process.

In order to characterize the Bi_2Te_3/GQDs interface, XPS analysis for the as-prepared Bi_2Te_3/GQDs2 and corresponding SPS bulk were performed. As shown in Figure 4a, the C 1s

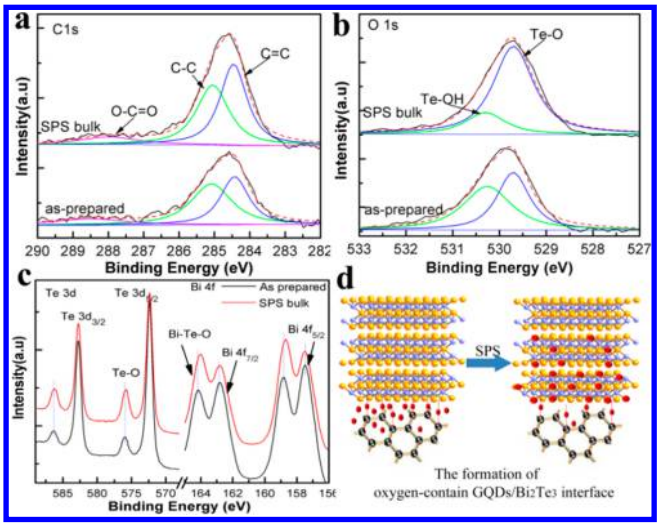

Figure 4. XPS spectra for the as-prepared Bi_2Te_3/GQDs2 and corresponding bulk sample after SPS sintering: (a) C 1s peak; (b) O 1s peak; and (c) Te 3d and Bi 4f peaks. (d) Schematic of the formation of the oxygen-containing Bi_2Te_3/GQDs interface.

peaks of both samples are reasonably decomposed into three peaks with binding energies of 287.9 eV (O—C═O), 286.2 eV (C—C), and 284.9 eV (C═C), respectively. The O 1s region shows the tellurium oxide peak at 529.7 eV (Te—O) as well as

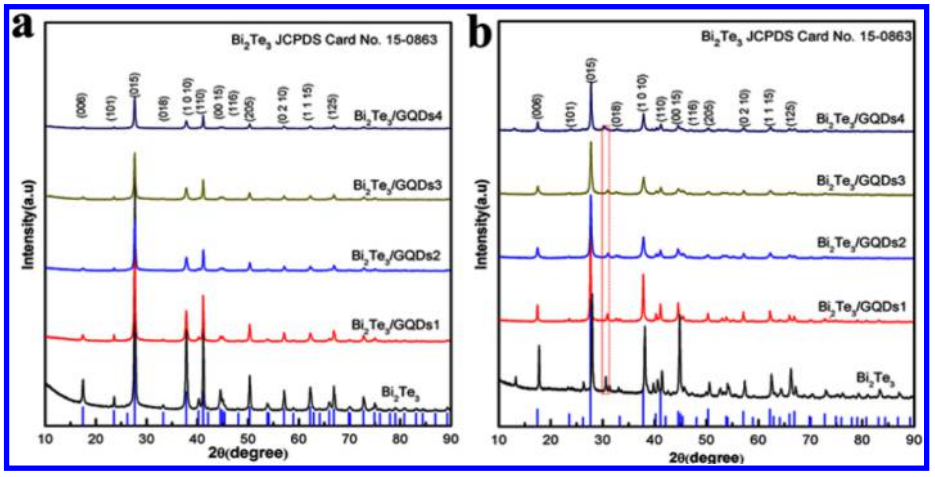

Figure 3. XRD patterns of the Bi_2Te_3/GQDs hybrid nanosheets with different GQD contents: (a) the as-prepared and (b) after SPS process.

DOI: 10.1021/acsami.6b14274
ACS Appl. Mater. Interfaces 2017, 9, 3677−3685

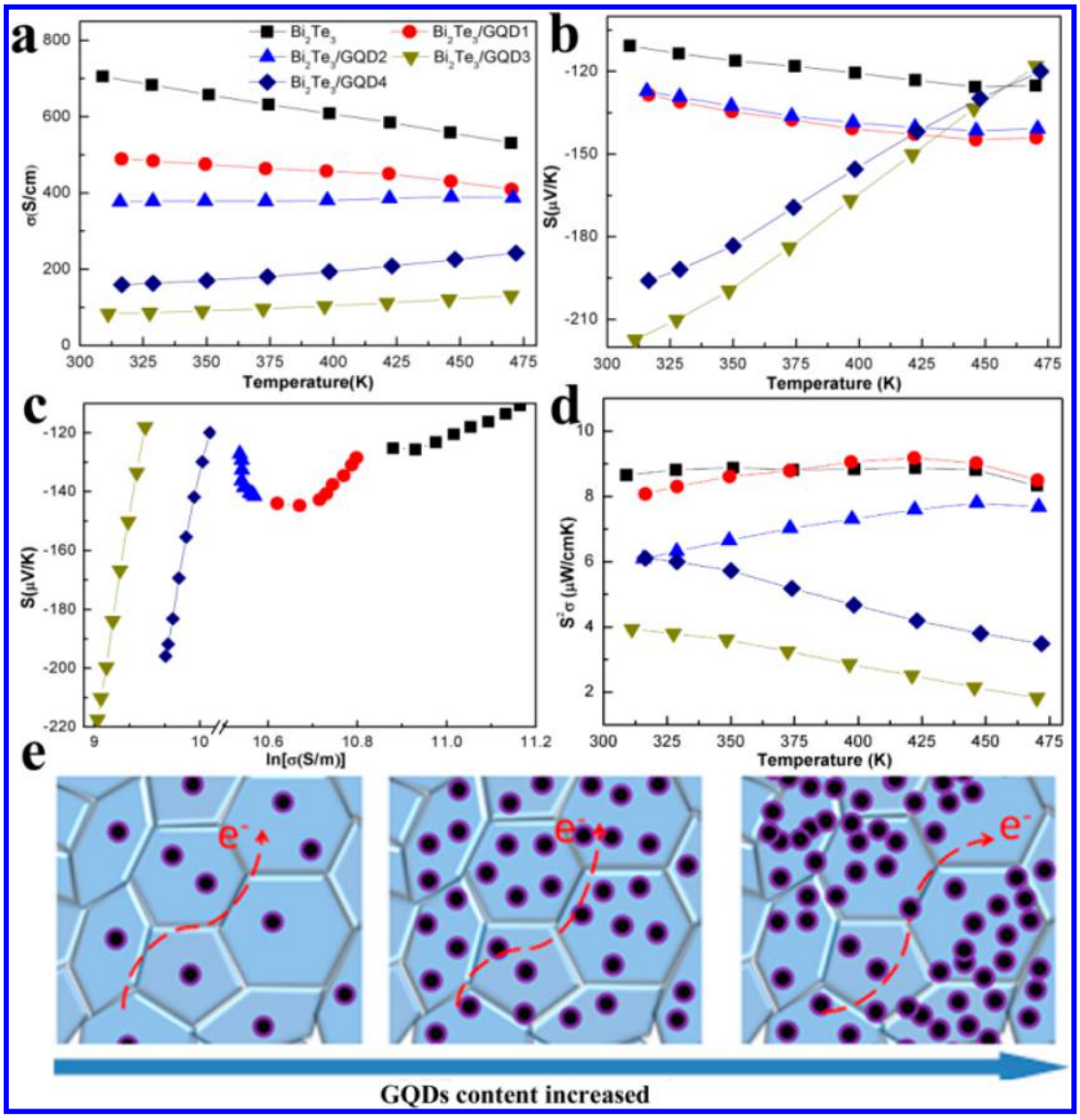

Figure 5. Thermoelectric properties of the Bi_2Te_3/GQDs samples with different GQDs contents: (a) electrical conductivity (σ); (b) Seebeck coefficient (S); (c) Seebeck coefficient as a function of the natural logarithm of the electrical conductivity; and (d) power factor ($S^2\sigma$). (e) Sketch of the electronic transmission path in the Bi_2Te_3/GQDs hybrid with different GQDs contents.

the tellurium hydroxyl peak at 530.4 eV (Te—OH), which all related to the surface oxidation of Te atoms on the Bi_2Te_3/GQDs interface. Remarkably, the intesity of the Te—OH peak decreases significantly, and the intensity of the Te—O peak increases for the bulk sample after SPS sintering, implying that the Te—OH peak transforms into the Te—O peak, which could be attributed to the diffusion of O atoms from the Bi_2Te_3/GQDs interface to the Bi_2Te_3 matrix.[20,21] This is consistent with the fact that the peak related to oxidation appears on the XRD pattern. The Te 3d region (Figure 4c) shows that the Te $3d^5/_2$ and $3d^3/_2$ peaks are located at 572.0 and 582.3 eV, respectively. The peaks of the Te—O species related to the surface oxidation of Te atoms were located at 575.6 and 586.2 eV.[20] The Bi 4f region also shows the Bi $4f^5/_2$ and Bi $4f^7/_2$ as well as the corresponding Bi—Te—O peaks. Importantly, after SPS sintering, both the Te—O and Bi—Te—O peaks shift toward high binding energy, which is also evidence that the O atoms of oxygen-functional groups at GQDs surface diffuse from the Bi_2Te_3/GQDs interface to the Bi_2Te_3 matrix. The oxygen-containing Bi_2Te_3/GQDs interface is the key factor to improve the thermoelectric transport properties of the Bi_2Te_3/GQDs hybrid nanosheets. There are three most common types of defects for the Bi_2Te_3-based alloys, including antisite defects of Bi in Te sites (contributes one hole per defect), vacancies at the Te sites (contributes two electrons per defect), and vacancies at Bi sites (contributes three holes per defect). As to the Bi_2Te_3 nanostructure, the enormous dangling bonds at grain boundaries would lead to the generation of Te vacancies resulting in n-type thermoelectric properties.[33] For the Bi_2Te_3/GQDs hybrid nanosheets, the O doping at the Bi_2Te_3/GQDs interface usually increases the concentration of Te vacancies and hence gives more electrons because of the lower energy of evaporation of O. Therefore, the Bi_2Te_3/GQDs interfaces play an important role to optimize regulation of the thermoelectric transport properties of the sample.

The transport properties of Bi_2Te_3/GQDs hybrid nanosheets were measured in the temperature range 300−480 K, as shown in Figure 5a. Pure Bi_2Te_3 has a very high electrical conductivity of ∼720 S/cm at room temperature, comparable to the

DOI: 10.1021/acsami.6b14274
ACS Appl. Mater. Interfaces 2017, 9, 3677−3685

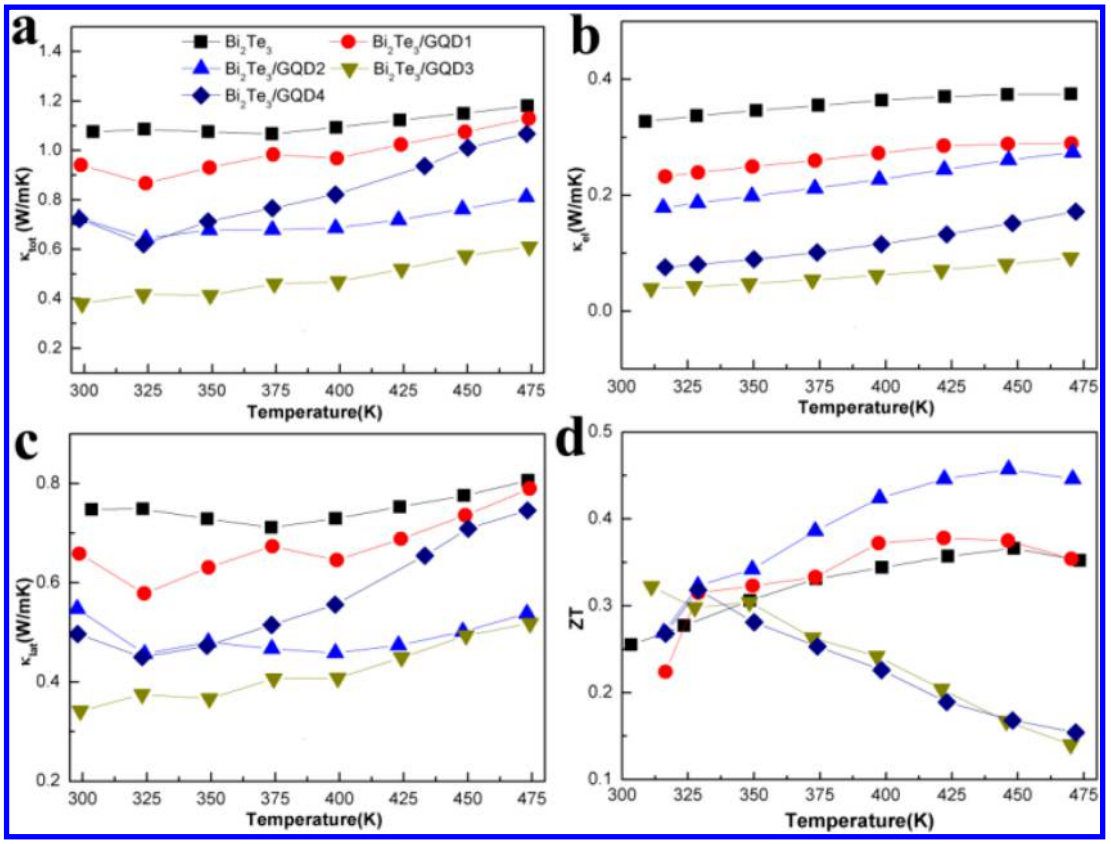

Figure 6. Temperature-dependence of (a) total thermal conductivity; (b) electronic thermal conductivities (κ_{el}) (estimated from the Wiedemann–Franz law); (c) lattice thermal conductivity (κ_{latt}); and (d) thermoelectric figure of merit of the as-prepared samples.

reported Bi_2Te_3-nanostructured bulk materials.[22−24] With the increasing of x, the electrical conductivity decreases systematically, which clearly demonstrates the important role of the Bi_2Te_3/GQDs interface. The high-density Bi_2Te_3/GQDs interface could enhance carrier scattering and decrease carrier mobility, giving rise to the decrease in electrical conductivity. It is observed that, for pure Bi_2Te_3, Bi_2Te_3/GQDs1, and Bi_2Te_3/GQDs2, the electrical conductivities decrease with increasing temperature, indicating a metallic transport behavior, which is similar to some previous reports.[25] On the other hand, for the samples with a high content of GQDs, the electrical conductivities increase with increasing temperature; this is a typical semiconductor behavior. The transformation of electron transport characteristics with the increasing of the GQDs content could be attributed to the increased contribution of carrier scattering arising from the charged Bi_2Te_3/GQDs interface. As mentioned above, the O-doping usually increases the concentration of Te vacancies, which results in the formation of the charged donorlike Bi_2Te_3/GQDs interface. This charged Bi_2Te_3/GQDs interface could inject excess charge carriers into the core of the Bi_2Te_3 grain, resulting in an increase of the carrier concentration. Moreover, the charged Bi_2Te_3/GQDs interface leads to selective scattering of holes over electrons due to increased coulomb barriers. For the sample with high GQDs content, such interface potential barrier scattering of carriers is the dominant scattering mechanism because of high density of interfaces. Then, the electrical conductivity can be expressed as

$$\sigma(T) \sim \frac{1}{\sqrt{T}} \exp\left(-\frac{e\phi_a}{k_B T}\right)$$

where ϕ_a is the height of the interface potential barrier due to the above-mentioned interfacial charged defects and k_B is the Boltzmann constant.[34] Similar charged interface dominated carrier transport behaviors have been extensively studied in various nanomaterials.[35]

The negative Seebeck coefficient of all samples reveals a n-type electrical transport behavior, which is in agreement with the previous reports on Bi_2Te_3-based nanostructures.[26] The absolute value of S increases from 110 to 140 μV K^{-1} for the samples with low GQDs content, which is comparable to the reported Bi_2Te_3-nanostructured bulk materials.[27,28] In contrast, for the sample with high GQDs content, the absolute value of S decreases significantly from 220 to 110 μV K^{-1} as the temperature increases. For n-type single-band approximation and a nondegenerate semiconductor, the Seebeck coefficient and the electrical conductivity can be expressed as[29]

$$S = -\frac{k_B}{e}\left[\left(r + \frac{5}{2}\right) - \xi\right]$$

$$\sigma = 2e\left(\frac{2\pi m_0 k_B T_0}{h^2}\right)^{3/2}\left(\frac{T}{T_0}\right)^{3/2}(m^*/m_0)^{3/2}\mu \exp(\xi)$$

where ξ, h, r, m_0, and T_0 are the reduced Fermi energy, Planck constant, scattering factor, free electron mass, and room temperature, respectively. Meanwhile, the Seebeck coefficient could be expressed as a function of the natural logarithm of the electrical conductivity[29]

$$S = -\frac{k_B}{e}\left[A + \frac{3}{2}\ln\left(\frac{T}{T_0}\right) + \ln U - \ln \sigma\right]$$

DOI: 10.1021/acsami.6b14274
ACS Appl. Mater. Interfaces 2017, 9, 3677−3685

where A is a scattering factor related parameter and U is the weighted mobility that is defined as $(m^*/m_0)^{3/2}\mu$. For a given system with different Fermi energy, the value $\partial S/\partial \ln(\sigma)$ should be a classic value k_B/e (~86.2 μV K^{-1}).[30] By plotting the Seebeck coefficient of Bi_2Te_3/GQDs hybrids as a function of the natural logarithm of the electrical conductivity, it is shown clearly that both values significantly deviate from the classic result, indicating that the carrier effective mass m^* or carrier mobility μ is considerably affected by the above-mentioned Bi_2Te_3/GQDs interface potential barrier.

Therefore, GQDs play multiple roles, including nucleation center, impurity and electron donor, which have a complex impact on the electronic properties of Bi_2Te_3/GQDs hybrids. A combination of these interactions between composites and carriers could be employed to understand the novel behavior of the Bi_2Te_3/GQDs hybrids. In the sample with low GQDs content (x = 1 and 2), the electron scattering caused by the Bi_2Te_3 grain boundary is stronger than the Bi_2Te_3/GQDs interfaces because of the relatively low number density of GQDs, which results in a typical metallic behavior similar to pure Bi_2Te_3. However, in the sample with high GQDs content (the number density of GQDs is about 10^{18} cm^{-3}), the Bi_2Te_3/GQDs interface potential barrier scattering of carriers is the dominant scattering mechanism, which gives rise to the transformation of electron transport characteristics. Furthermore, it should be noted that the agglomeration of the GQDs can be clearly observed in the FE-SEM images (Figure S4) of the fractured surfaces of the sample with high GQDs content (Bi_2Te_3/GQDs4), which is in agreement with the fact that the electrical conductivity of Bi_2Te_3/GQDs4 is slightly higher than that of Bi_2Te_3/GQDs3. The power factor of Bi_2Te_3/GQDs1 shows a maximum value of 9.2 μW cm^{-1} K^{-2} at 425 K, which is slightly higher than that of pure Bi_2Te_3 (8.9 μW cm^{-1} K^{-2} at 425 K), indicating an optimization of the carrier transport characteristics by introducing hybrid nanostructure. Thus, the Bi_2Te_3/GQDs interfaces play an important role to optimize the thermoelectric transport properties of Bi_2Te_3/GQDs hybrids, which could be further optimized by modifying the GQDs surface, such as reducing with hydrazine, adsorbing the transition metal ion or metal-free chalcogenides, and chemical treatment with various organic groups.

As expected, the hybrid nanostructure can significantly reduce the thermal conductivity, as shown in Figure 6a. Both Bi_2Te_3/GQDs hybrids possess extremely low thermal conductivity, which is significantly lower than that of pure Bi_2Te_3 (1.06 W m^{-1} K^{-1} at 300 K) in the same temperature range. The lowest κ_{tot} of 0.38 W m^{-1} K^{-1} at 300 K is obtained for Bi_2Te_3/GQDs3, which is one of the lowest values close to the predicted minimum thermal conductivity (0.31 W m^{-1} K^{-1}) in nanograined Bi_2Te_3 calculated using the Debye−Callaway model.[31,32] The total thermal conductivity can be expressed as $\kappa_{tot} = \kappa_{el} + \kappa_{latt}$, where κ_{el} and κ_{latt} are the electron and lattice thermal conductivities, respectively. According to the Wiedemann−Franz law, the electron thermal conductivity can be estimated using $\kappa_{el} = L\sigma T$, where L is the Lorentz number; 1.50 × 10^{-8} W Ω K^{-2} is used to calculate the electron contribution due to the nondegenerate feature of both pellets.[33] It is found that the electron contribution is quite minor in all samples because of the relatively low electrical conductivity. By introuducing hybrid nanostructure, the κ_{latt} is sharply reduced to about 0.3−0.5 W m^{-1} K^{-1}, which is much lower than that of pure Bi_2Te_3 (0.7−0.8 W m^{-1} K^{-1}). It should be pointed out that both the κ_{tot} and κ_{latt} decrease with the GQDs content, which could be attributed to the increasing of the Bi_2Te_3/GQDs interface and grain boundaries. Moreover, the thermal conductivity of Bi_2Te_3/GQDs3 is slightly lower than that of Bi_2Te_3/GQDs4, which agrees with the trend that the GQDs are assembled in the sample with high GQDs content. Compared to pure Bi_2Te_3, the Bi_2Te_3/GQDs hybrid samples, especially Bi_2Te_3/GQDs4, show an evident difference in k_{latt}, indicating the presence of an additional scattering process, which is consistent with interfacial charged defect scattering. Because of the significant reduction of κ_{latt} by strong phonon scattering at high density defects, Bi_2Te_3/GQDs interface and grain boundaries, highly improved thermoelectric performance has been achieved. The maximum ZT value reaches 0.46 at 450 K for Bi_2Te_3/GQDs2, which is significantly improved compared to that of pure Bi_2Te_3 nanosheets (0.37 at 450 K).

On the basis of the above discussion, the enhanced thermoelectric performance of Bi_2Te_3/GQDs hybrids is mainly due to the significantly reduced κ_{latt} by strong phonon scattering at high-density grain boundaries, Bi_2Te_3/GQDs interface and defects. To understand the impact of microstructures on our remarkably low κ_{latt}, TEM investigation has been employed to analyze the structural characteristics of the SPS pellets. TEM images (Figure 7) reveal the random stacking

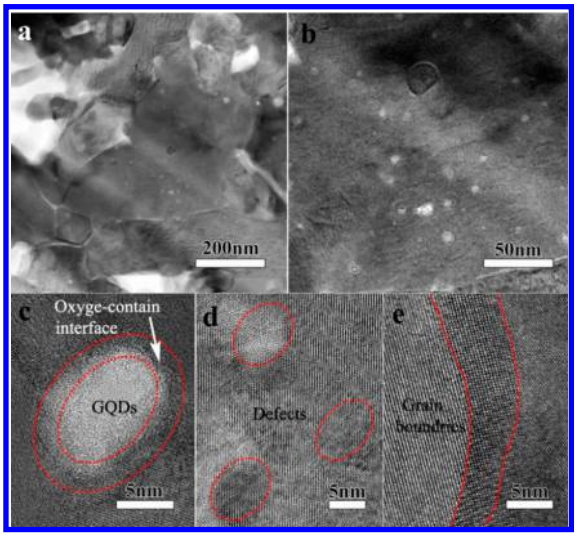

Figure 7. (a) TEM images of the Bi_2Te_3/GQDs hybrid bulk after SPS sintering; (b) TEM image of the Bi_2Te_3/GQDs hybrid showing the GQDs uniformly dispersed in the bulk matrix; (c, d, e) HR-TEM images of the different regions.

of nanosized grains with clear grain boundaries, suggesting the multigrain feature of our pellets. Interestingly, TEM images of Bi_2Te_3/GQDs2 show the GQDs with high density (~1 × 10^{11} cm^{-2} confirmed by extensive HR-TEM analyses) are evenly dispersed in the bulk matrix (Figure 7b), which agree with the above discussion. Moreover, as presented earlier, the Bi_2Te_3/GQDs interface with 1−2 nm thickness amorphous regions could be clearly observed in the HR-TEM image. The formation of this amorphous interface could be attributed to the diffusion of an excessive number of oxygen atoms near the GQDs surface to the Bi_2Te_3 matrix during the sintering process, which has been discussed above. Furthermore, the nanoscale grain boundaries appear clearly in Figure 7d. Moreover, a high density of nanoscale distorted regions and atomic scale distortions, such as tiny distorted regions and dislocations (marked with red lines in Figure 7d) are observed in the

DOI: 10.1021/acsami.6b14274
ACS Appl. Mater. Interfaces 2017, 9, 3677−3685

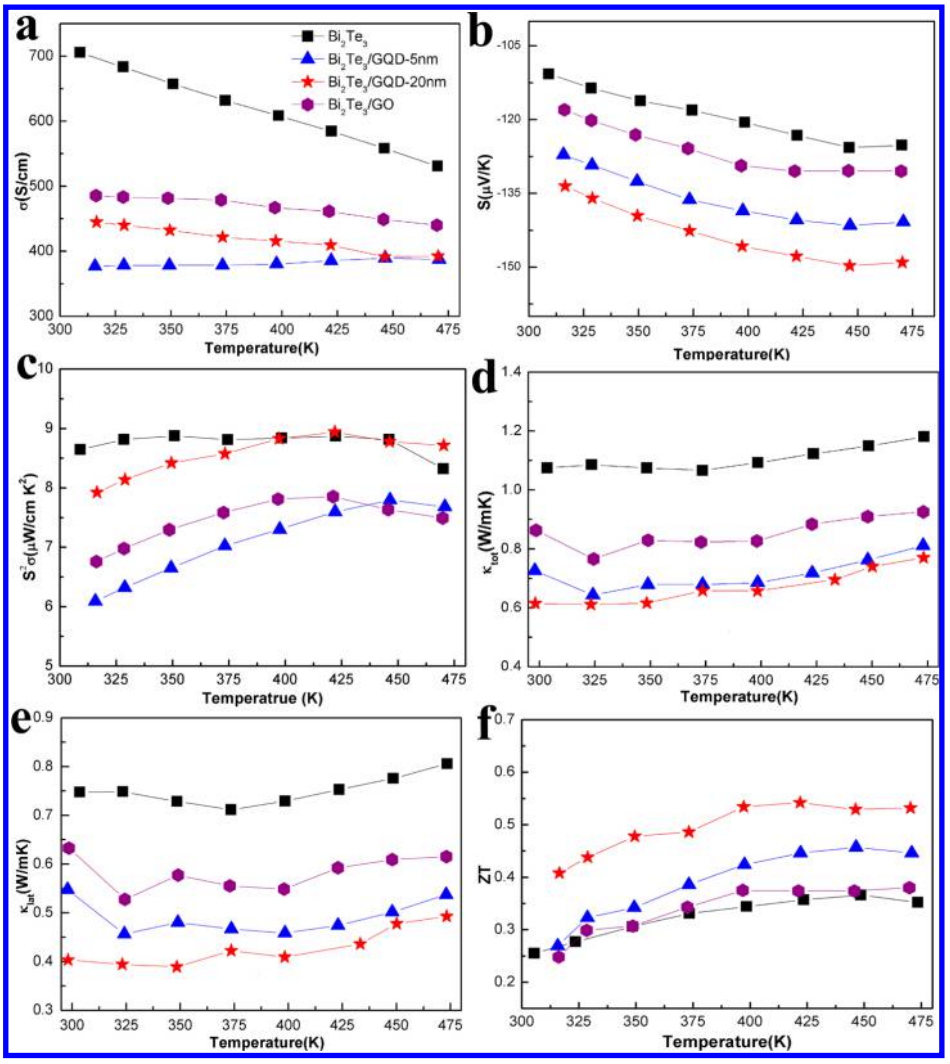

Figure 8. Thermoelectric properties of the Bi_2Te_3/GQDs hybrid nanosheets with different GQDs size: (a) electrical conductivity (σ); (b) Seebeck coefficient (S); (c) power factor ($S^2\sigma$); (d) total thermal conductivity (κ_{tot}); (e) lattice thermal conductivity (κ_{latt}); and (f) thermoelectric figure of merit (ZT).

sintered pellets. Such a high-density Bi_2Te_3/GQDs interface, coupled with various atomic scale defects and nanoscale grain boundaries, can greatly enhance phonon scattering to target the wide spectrum of phonons to maximum reduction in κ_{latt}.

Therefore, the introduction of Bi_2Te_3/GQDs hybrid nanostructure has been demonstrated to be a rational approach to improve the thermoelectric performance of Bi_2Te_3-based nanomaterials. The enhanced thermoelectric performance is caused by the optimized carrier and phonon transport characteristics by the Bi_2Te_3/GQDs interface, which can be regulated in the future by varying the size of the GQDs. It would be interesting to investigate how the size of the GQDs regulates the carrier and phonon transport characteristics of the hybrid nanostructures. Therefore, two sizes of GQDs, GQDs-5 nm (average size about 5 nm) and GQDs-20 nm (average size about 20 nm), as well as graphene oxide (GO) have been used to synthesize Bi_2Te_3/GQDs hybrids. All of the Bi_2Te_3/GQDs hybrids have the same GQDs content (2 mL of GQDs solution (4 mg/mL)), which is the optimum content for the GQDs-5 nm as discussed above. Figure 8a presents σ and S of the as-prepared Bi_2Te_3/GQDs hybrids as a function of temperature. For all samples, the electrical conductivities decrease with increasing temperature due to the low GQDs content, which agrees with the previous discussion. As can be seen, the Bi_2Te_3/GQDs-20 nm shows a much higher electrical conductivity (440−390 S cm^{-1}) as well as higher Seebeck coefficient (−130 ∼ −150 $\mu V\ K^{-1}$) than that of Bi_2Te_3/GQDs-5 nm and Bi_2Te_3/GO. Meanwhile, both the electrical conductivity and Seebeck coefficient of Bi_2Te_3/GQDs-5 nm show a relatively gentle change trend with the increase of temperature, indicating the increased contribution of carrier scattering arising from the charged Bi_2Te_3/GQDs interface due to a high Bi_2Te_3/GQDs interface area caused by small GQDs size. The power factor of the Bi_2Te_3/GQDs-20 nm is about 8.9 $\mu W\ cm^{-1}\ K^{-2}$ at 425 K, which is higher than that of GQDs-5 nm and Bi_2Te_3/GO. However, The κ_{tot} of Bi_2Te_3/GQDs-20 nm is lower than that of the other two competitors due to the low κ_{latt}, which is inconsistent with the fact that Bi_2Te_3/GQDs-5 nm has more Bi_2Te_3/GQDs interfaces than Bi_2Te_3/GQDs-20 nm. The mechanism accounting for such enhanced phonon scattering may be complicated. Besides the aforementioned density of the Bi_2Te_3/GQDs interfaces, the dispersion manner of GQDs in the Bi_2Te_3 matrix may also play an important role in affecting the phonon scattering. It is evident that the GQDs are uniformly dispersed in the bulk matrix for Bi_2Te_3/GQDs-5 nm while the GO is dispersed at grain boundaries for Bi_2Te_3/GO

DOI: 10.1021/acsami.6b14274
ACS Appl. Mater. Interfaces 2017, 9, 3677−3685

(Figure S5). Therefore, for Bi_2Te_3/GQDs-20 nm, the GQDs may be dispersed in both nanograins and boundaries, resulting in the enhanced phonon scattering. Besides electron doping and the carrier filtering effect, the quantum confinement effect of GQDs may also contribute substantially to the enhanced thermoelectric performance of Bi_2Te_3/GQDs hybrids due to the small size of GQDs. Because of the enlarged power factor and simultaneously decreased κ_{tot}, ZT for Bi_2Te_3/GQDs-20 nm reaches ~0.55, much larger than that of ~0.46 for Bi_2Te_3/GQDs-5 nm and 0.38 for Bi_2Te_3/GO. The maximum ZT for Bi_2Te_3/GQDs hybrid nanosheets (0.55 at 425 K) is comparable to most solution-synthesized n-type Bi_2Te_3 nanostructures, which could be greatly improved by introducing proper doping, such as Sb and Se.[6,7,21] Furthermore, the further prospect of this study is modifying the GQDs surface or varying the alignment and matrix deformation, which could improve the thermoelectric properties by regulation of the Bi_2Te_3/GQDs interfaces. The results of this study provide insight for the structural design and synthesis of hybrid thermoelectric materials, which will be important for future development of broadly functional material systems.

4. CONCLUSION

In summary, we successfully synthesized Bi_2Te_3/GQDs hybrid nanosheets via a simple solution-based approach. The GQDs with an oxygen-containing surface (−OH and −COOH) not only act as heterogeneous nucleation centers during the growth process but also act as the impurity and donor electron to construct the charged Bi_2Te_3/GQDs interface. The charged Bi_2Te_3/GQDs interface could affect the electron transport behavior by selective scattering of carriers due to increased coulomb barriers. Moreover, the high-density Bi_2Te_3/GQDs interface, coupled with various atomic scale defects and nanoscale grain boundaries, can greatly enhance phonon scattering to target the wide spectrum of phonons so as to maximum reduction in κ_{latt}. Taking advantage of the optimization to the carriers and phonon transport behavior, enhanced thermoelectric performance has been achieved. A maximum ZT of 0.55 is obtained at 425 K for the Bi_2Te_3/GQDs-20 nm, which is higher than that of the Bi_2Te_3 nanosheet without the hybrid nanostrucure. Furthermore, by varying the size of the GQDs, the thermoelectric performance of Bi_2Te_3/GQDs hybrid nanostructures could be further enhanced, which could be attributed to the optimization of the density and dispersion manner of GQDs in the Bi_2Te_3 matrix.

■ ASSOCIATED CONTENT

Supporting Information

The Supporting Information is available free of charge on the ACS Publications website at DOI: 10.1021/acsami.6b14274.

Figure S1, experimental section including the synthesis and characterization of the GQDs; Figure S2, SEM images of Bi_2Te_3 nanoplates; Figures S3 and S4, SEM images of the fractured surfaces of Bi_2Te_3/GQDsx; Figure S5, the fractured surfaces of Bi_2Te_3/GO and Bi_2Te_3/GQDs-20 nm; Table S1, volume density of all bulk samples (PDF)

■ AUTHOR INFORMATION

Corresponding Authors

*(Y.L.) E-mail: liuyd@pkusz.edu.cn.

*(F.P.) E-mail: panfeng@pkusz.edu.cn.

ORCID

Hong Meng: 0000-0001-5877-359X

Feng Pan: 0000-0002-8216-1339

Author Contributions

§(S.L. and T.F.) These authors contributed equally to this work. The manuscript was written through contributions of all authors. All authors have given approval to the final version of the manuscript.

Notes

The authors declare no competing financial interest.

■ ACKNOWLEDGMENTS

This work was financially supported by the National Materials Genome Project (2016YFB0700600), the Shenzhen Science and Technology Research Grant (nos. ZDSY20130331145131323, CXZZ20120829172325895, JCYJ20120614150338154, and JCYJ20150629144612861), and the China Postdoctoral Science Foundation (no. 2016M600862).

■ REFERENCES

(1) Han, C.; Sun, Q.; Li, Z.; Dou, S. X. Thermoelectric Enhancement of Different Kinds of Metal Chalcogenides. *Adv. Energy Mater.* **2016**, *6*, 1600498−1600536.

(2) Kanatzidis, M. G. Advances in Thermoelectrics: From Single Phases to Hierarchical Nanostructures and Back. *MRS Bull.* **2015**, *40*, 687−694.

(3) Heinz, N. A.; Ikeda, T.; Pei, Y.; Snyder, G. J. Applying Quantitative Microstructure Control in Advanced Functional Composites. *Adv. Funct. Mater.* **2014**, *24*, 2135−2153.

(4) Kim, H. S.; Wang, T.; Liu, W.; Ren, Z. Engineering Thermal Conductivity for Balancing Between Reliability and Performance of Bulk Thermoelectric Generators. *Adv. Funct. Mater.* **2016**, *26* (21), 3678−3686.

(5) Zeier, W. G.; Zevalkink, A.; Gibbs, Z. M.; Hautier, G.; Kanatzidis, M. G.; Snyder, G. J. Thinking Like a Chemist: Intuition in Thermoelectric Materials. *Angew. Chem., Int. Ed.* **2016**, *55*, 6826−6841.

(6) Zhang, G.; Kirk, B.; Jauregui, L. A.; Yang, H.; Xu, X.; Chen, Y. P.; Wu, Y. Rational Synthesis of Ultrathin n-Type Bi_2Te_3 Nanowires with Enhanced Thermoelectric Properties. *Nano Lett.* **2012**, *12*, 56−60.

(7) Guo, W.; Ma, J.; Yang, J.; Li, D.; Qin, Q.; Wei, C.; Zheng, W. A New Strategy for Realizing the Conversion of "Homo-Hetero-Homo" Heteroepitaxial Growth in Bi_2Te_3 and the Thermoelectric Performance. *Chem. - Eur. J.* **2014**, *20*, 5657−5664.

(8) Hong, M.; Chasapis, T. C.; Chen, Z.-G.; Yang, L.; Kanatzidis, M. G.; Snyder, G. J.; Zou, J. n-Type $Bi_2Te_{3-x}Se_x$ Nanoplates with Enhanced Thermoelectric Efficiency Driven by Wide-Frequency Phonon Scatterings and Synergistic Carrier Scatterings. *ACS Nano* **2016**, *10* (4), 4719−4727.

(9) Seo, S.; Lee, K.; Jeong, Y.; Oh, M.-W.; Yoo, B. Method of Efficient Ag Doping for Fermi Level Tuning of Thermoelectric $Bi_{0.5}Sb_{1.5}Te_3$ Alloys Using a Chemical Displacement Reaction. *J. Phys. Chem. C* **2015**, *119*, 18038−18045.

(10) Hong, M.; Chen, Z.-G.; Yang, L.; Zou, J. Enhancing Thermoelectric Performance of Bi_2Te_3-based Nanostructures through Rational Structure Design. *Nanoscale* **2016**, *8*, 8681−8686.

(11) Zhu, Y.; Murali, S.; Cai, W.; Li, X.; Suk, J.; Potts, J. R.; Ruoff, R. S. Graphene and Graphene Oxide: Synthesis, Properties, and Applications. *Adv. Mater.* **2010**, *22*, 3906−3924.

(12) Loh, K. P.; Bao, Q.; Eda, G.; Chhowalla, M. Graphene Oxide as a Chemically Tunable Platform for Optical Applications. *Nat. Chem.* **2010**, *2* (12), 1015−1024.

(13) Qi, Y.; Zhang, M.; Fu, Q.; Liu, R.; Shi, G. Highly Sensitive and Selective Fluorescent Detection of Cerebral Lead (II) Based on

DOI: 10.1021/acsami.6b14274
ACS Appl. Mater. Interfaces 2017, 9, 3677−3685

Graphene Quantum Dot Conjugates. *Chem. Commun.* **2013**, *49*, 10599−10601.
(14) Yuan, X.; Liu, Z.; Guo, Z.; Ji, Y.; Jin, M.; Wang, X. Cellular Distribution and Cytotoxicity of Graphene Quantum Dots with Different Functional Groups. *Nanoscale Res. Lett.* **2014**, *9*, 108.
(15) Scheele, M.; Oeschler, N.; Meier, K.; Kornowski, A.; Klinke, C.; Weller, H. Synthesis and Thermoelectric Characterization of Bi_2Te_3 Nanoparticles. *Adv. Funct. Mater.* **2009**, *19* (21), 3476−3483.
(16) Dresselhaus, M. S.; Chen, G.; Tang, M. Y.; Yang, R. G.; Lee, H.; Wang, D. Z.; Ren, Z. F.; Fleurial, J. P.; Gogna, P. New Directions for Low-Dimensional Thermoelectric Materials. *Adv. Mater.* **2007**, *19*, 1043−1053.
(17) Fan, T.; Zeng, W.; Tang, W.; Yuan, C.; Tong, S.; Cai, K.; Liu, Y.; Huang, W.; Min, Y.; Epstein, A. J. Controllable Size-selective Method to Prepare Graphene Quantum Dots from Graphene Oxide. *Nanoscale Res. Lett.* **2015**, *10*, 55−60.
(18) Liang, Y.; Lu, C.; Ding, D.; Zhao, M.; Wang, D.; Hu, C.; Qiu, J.; Xie, G.; Tang, Z. Capping Nanoparticles with Graphene Quantum Dots for Enhanced Thermoelectric Performance. *Chem. Sci.* **2015**, *6*, 4103−4108.
(19) Li, S.; Zheng, J.; Zuo, S.; Wu, Z.; Yan, P.; Pan, F. 2D Hybrid Anode based on SnS Nanosheet Bonded with Graphene to Enhance Electrochemical Performance for Lithium-ion Batteries. *RSC Adv.* **2015**, *5* (58), 46941−46946.
(20) Thomas, C. R.; Vallon, M. K.; Frith, M. G.; Sezen, H.; Kushwaha, S. K.; Cava, R. J.; Schwartz, J.; Bernasek, S. L. Surface Oxidation of $Bi_2(Te,Se)_3$ Topological Insulators Depends on Cleavage Accuracy. *Chem. Mater.* **2016**, *28* (1), 35−39.
(21) Yashina, L. V.; Sánchez-Barriga, J.; Scholz, M. R.; Volykhov, A. a.; Sirotina, A. P.; Neudachina, V. S.; Tamm, M. E.; Varykhalov, A.; Marchenko, D.; Springholz, G.; Bauer, G.; Knop-Gericke, A.; Rader, O. Negligible Surface Reactivity of Topological Insulators Bi_2Se_3 and Bi_2Te_3 Towards Oxygen and Water. *ACS Nano* **2013**, *7*, 5181−5191.
(22) Han, G.; Chen, Z.-G.; Yang, L.; Hong, M.; Drennan, J.; Zou, J. Rational Design of Bi_2Te_3 Polycrystalline Whiskers for Thermoelectric Applications. *ACS Appl. Mater. Interfaces* **2015**, *7* (1), 989−995.
(23) Stavila, V.; Robinson, D. B.; Hekmaty, M. A.; Nishimoto, R.; Medlin, D. L.; Zhu, S.; Tritt, T. M.; Sharma, P. A. Wet-Chemical Synthesis and Consolidation of Stoichiometric Bismuth Telluride Nanoparticles for Improving the Thermoelectric Figure-of-Merit. *ACS Appl. Mater. Interfaces* **2013**, *5*, 6678−6686.
(24) Son, J. S.; Zhang, H.; Jang, J.; Poudel, B.; Waring, A.; Nally, L.; Talapin, D. V. All-Inorganic Nanocrystals as a Glue for BiSbTe Grains: Design of Interfaces in Mesostructured Thermoelectric Materials. *Angew. Chem., Int. Ed.* **2014**, *53*, 7466−7470.
(25) Zhang, Y.; Day, T.; Snedaker, M. L.; Wang, H.; Krämer, S.; Birkel, C. S.; Ji, X.; Liu, D.; Snyder, G. J.; Stucky, G. D. A Mesoporous Anisotropic n-Type Bi_2Te_3 Monolith with Low Thermal Conductivity as an Efficient Thermoelectric Material. *Adv. Mater.* **2012**, *24*, 5065−5070.
(26) Schumacher, C.; Reinsberg, K. G.; Rostek, R.; Akinsinde, L.; Baessler, S.; Zastrow, S.; Rampelberg, G.; Woias, P.; Detavernier, C.; Broekaert, A. C.; Bachmann, J.; Nielsch, K. Optimizations of Pulsed Plated p and n-type Bi_2Te_3-Based Ternary Compounds by Annealing in Different Ambient Atmospheres. *Adv. Energy Mater.* **2013**, *3*, 95−104.
(27) Son, J. S.; Choi, M. K.; Han, M.-K.; Park, K.; Kim, J.-Y.; Lim, S. J.; Oh, M.; Kuk, Y.; Park, C.; Kim, S.-J.; Hyeon, T. n-Type Nanostructured Thermoelectric Materials Prepared from Chemically Synthesized Ultrathin Bi_2Te_3 Nanoplates. *Nano Lett.* **2012**, *12*, 640−647.
(28) Hu, L.; Wu, H.; Zhu, T.; Fu, C.; He, J.; Ying, P.; Zhao, X. Tuning Multiscale Microstructures to Enhance Thermoelectric Performance of n-Type Bismuth-Telluride-Based Solid Solutions. *Adv. Energy Mater.* **2015**, *5*, 1500411−1500423.
(29) Mehdizadeh Dehkordi, A.; Bhattacharya, S.; Darroudi, T.; Graff, J. W.; Schwingenschlögl, U.; Alshareef, H. N.; Tritt, T. M. Large Thermoelectric Power Factor in Pr-Doped $SrTiO_{3-\delta}$ Ceramics via Grain-Boundary-Induced Mobility Enhancement. *Chem. Mater.* **2014**, *26*, 2478−2485.
(30) Liu, W.-S.; Zhang, B.-P.; Zhao, L.-D.; Li, J.-F. Improvement of Thermoelectric Performance of $CoSb_{3-x}Te_x$ Skutterudite Compounds by Additional Substitution of IVB-Group Elements for Sb. *Chem. Mater.* **2008**, *20*, 7526−7531.
(31) Li, S.; Xin, C.; Liu, X.; Feng, Y.; Liu, Y.; Zheng, J.; Liu, F.; Huang, Q.; Qiu, Y.; He, J.; Luo, J.; Pan, F. 2D Hetero-nanosheets to Enable Ultralow Thermal Conductivity by All Scale Phonon Scattering for Highly Thermoelectric Performance. *Nano Energy* **2016**, *30*, 780−789.
(32) Takashiri, M.; Tanaka, S.; Hagino, H.; Miyazaki, K. Combined Effect of Nanoscale Grain Size and Porosity on Lattice Thermal Conductivity of Bismuth-telluride-based Bulk Alloys. *J. Appl. Phys.* **2012**, *112*, 084315−084323.
(33) Liu, W.-S.; Zhang, Q.; Lan, Y.; Chen, S.; Yan, X.; Zhang, Q.; Wang, H.; Wang, D.; Chen, G.; Ren, Z. Thermoelectric Property Studies on Cu-Doped n-type $Cu_xBi_2Te_{2.7}Se_{0.3}$ Nanocomposites. *Adv. Energy Mater.* **2011**, *1*, 577−587.
(34) Puneet, P.; Podila, R.; Karakaya, M.; Zhu, S.; He, J.; Tritt, T. M.; Dresselhaus, M. S.; Rao, A. M. Preferential Scattering by Interfacial Charged Defects for Enhanced Thermoelectric Performance in Few-layered n-type Bi_2Te_3. *Sci. Rep.* **2013**, *3*, 1−7.
(35) Han, M.-K.; Kim, S.; Kim, H.-Y.; Kim, S.-J. An Alternative Strategy to Construct Interfaces in Bulk Thermoelectric Material: Nanostructured Heterophase Bi_2Te_3/Bi_2S_3. *RSC Adv.* **2013**, *3*, 4673−4679.

DOI: 10.1021/acsami.6b14274
ACS Appl. Mater. Interfaces 2017, 9, 3677−3685